Nonlinear adjustment of a front over escarpment

F. Bouchut,[1] E. Scherer,[2] and V. Zeitlin[2,a)]
[1]*DMA, Ecole Normale Supérieure, 45, rue d'Ulm, 75230 Paris Cedex 05, France*
[2]*LMD, Ecole Normale Supérieure, 24, rue Lhomond, 75231 Paris Cedex 05, France*

(Received 25 June 2007; accepted 20 December 2007; published online 29 January 2008)

We present the results of fully nonlinear numerical simulations of the geostrophic adjustment of a pressure front over topography, represented by an escarpment with a linear slope. The results of earlier simulations in the linear regime are confirmed and new essentially nonlinear effects are found. Topography influences both fast and slow components of motion. The fast unbalanced motion corresponds to inertia-gravity waves (IGW). The IGW emitted during initial stages of adjustment break and form the localized dissipation zones. Due to topography, the IGW activity is enhanced in certain directions. The slow balanced motion corresponds to topographic Rossby waves propagating along the escarpment. As shown, at large enough nonlinearities they may trap fluid/tracer and carry it on. There are indications that nonlinear topographic waves form a soliton train during the adjustment process. If the coastal line is added to the escarpment at the shallow side (continental shelf), secondary fronts related to the propagation of the coastal Kelvin waves appear. © *2008 American Institute of Physics*. [DOI: 10.1063/1.2834731]

I. INTRODUCTION

The relaxation of a pressure front over topography (which is represented by an escarpment in a simplest, but practically important situation, see below) in a rotating fluid is a classical geophysical fluid dynamics problem. In the case of abrupt (step-function) escarpment it was treated analytically, in the linear approximation, and by means of laboratory experiments in the pioneering paper by Gill, Davey, Johnson, and Linden.[1] Complete linear analysis of the problem was achieved by Johnson and Davey[2] for a step-function escarpment of small amplitude in the unbounded domain and in the presence of the coast. Numerical analysis of the linear relaxation problem in the case of escarpment with a linear slope was performed by Allen.[3] The standard framework for studying the relaxation of the front is the rotating shallow water (RSW) model with topography. In the general perspective, the problem belongs to the "dam-break" class, well known in hydraulics. A thorough study of such a process in the presence of rotation, but without topography, was performed by Kuo and Polvani.[4] In the geophysical fluid dynamics perspective, the relaxation of a front is a geostrophic adjustment problem, as the velocity and the pressure fields should arrive to the geostrophically balanced state by inertia-gravity wave emission. It is, thus, a natural generalization of a classical Rossby problem of the adjustment of a jet.[5] The geostrophic adjustment of jets and fronts in RSW was extensively studied recently both analytically[6] and numerically.[7] The use of the new generation of high-resolution finite-volume codes for shallow-water equations allowed us to make substantial progress.[4,7]

In the present paper, we undertake a numerical study of the problem of fully nonlinear geostrophic adjustment of a pressure front over escarpment with a linear slope. Both the cases of an escarpment far from the coast and close to the coast will be considered. Unlike the previous theoretical and numerical studies, we are able to treat arbitrary nonlinearities. We use in our study the high-resolution, shock-capturing finite-volume method of Bouchut[8,9] (see Ref. 7 for a brief description). The advantage of the code is that it is well balanced, i.e., it maintains the geostrophic equilibria in the presence of topography.

The essence of the geostrophic adjustment process is that the flow starting from any localized initial condition is split into balanced (vortex, jets) and unbalanced [inertia-gravity waves (IGW)] parts.[10] The IGW carry the excess of energy away from the location of the initial perturbation while the balanced part slowly evolves, remaining close to the geostrophic equilibrium. In the case of initially plane-parallel jets/fronts, the balanced state is just stationary.[5,6] The new phenomena expected in the process of adjustment of the pressure front over escarpment are, first, related to the fact that topography destroys the one-dimensionality of the problem (escarpment is perpendicular to the pressure gradient), and thus the emitted inertia-gravity waves have different speeds at the shallow and deep sides of the escarpment, and therefore the wave-fronts will be curved. Besides, the attainability of the fully adjusted stationary state with a constant fluid depth all along the escarpment[1] is questionable. Presumably, the nonstationary intermediate balanced states should arise. Second, the presence of topographic Rossby (or double-Kelvin) waves introduces a completely new element in the problem, because these waves can move only in the prescribed along-escarpment direction.[11] They are balanced, and thus may be part of the just mentioned nonstationary balanced state. The wave-trapping phenomenon should modify the standard scenario of adjustment, given in Ref. 10 and 6. In this respect, the adjustment of the front over topography bears a resemblance to the equatorial adjustment, cf. Ref. 12. Both equator and topography act as waveguides for

a)Author to whom correspondence should be addressed. Electronic mail: zeitlin@lmd.ens.fr.

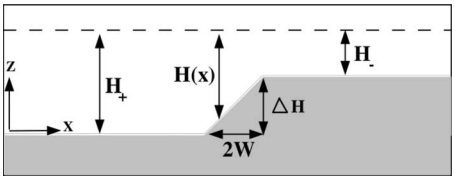

FIG. 1. The side view of the escarpment. The nonperturbed free surface is indicated by the dashed line.

some types of waves. It was demonstrated that nonlinear equatorial Rossby waves can provide anomalous transport of tracers.[13] One can ask whether a similar phenomenon may take place in the topographic waveguide. We will show that this is indeed the case for nonlinear topographic waves that form soliton-like structures with recirculation zones at strong enough nonlinearities.

We present below the results of numerical simulations of the nonlinear adjustment of a pressure front over topography for small and strong nonlinearities with and without an adjacent coast line, with special emphasis on the mixing and transport properties of the adjustment process. We also discuss the effects of the steepness of the slope. The Appendix contains a demonstration of the existence of the solitons of topographically trapped waves in a certain regime of parameters.

II. THE MODEL AND THE NUMERICAL SETUP

We work in the framework of nonlinear rotating shallow water model on the f plane in the presence of topography. The equations of the model are

$$u_t + uu_x + vu_y - fv = -g\eta_x, \tag{1}$$

$$v_t + uv_x + vv_y + fu = -g\eta_y, \tag{2}$$

$$\eta_t + [(H+\eta)u]_x + [(H+\eta)v]_y = 0, \tag{3}$$

where $u(x,y,t)$ is the zonal velocity, $v(x,y,t)$ is the meridional velocity, $H(x)$ is the fluid depth at rest, $\eta(x,y,t)$ is the free-surface elevation, and f is the Coriolis parameter, which we assume to be constant and positive. We consider a simple bathymetry consisting of a linear slope of width $2W$ connecting two flat regions with a depth difference along the x axis, $H_- - H_+ = \Delta H$; cf. Fig. 1.

Using the maximum depth of the fluid at rest H_+ as a vertical scale, the Rossby deformation radius $R_d = \sqrt{gH_+/f^2}$ as a typical horizontal scale, the inverse Coriolis parameter f^{-1} as a time scale, and introducing a typical velocity scale U and a typical value of the perturbation of the free surface $\Delta\eta$, we nondimensionalize the dependent and independent variables as follows:

$$x = \tilde{x}R_d, \quad y = \tilde{y}R_d, \quad W = \tilde{W}R_d, \quad H = \tilde{H}H_+,$$
$$\Delta H = \Delta\tilde{H}H_+, \quad \eta = \tilde{\eta}\Delta\eta, \tag{4}$$

$$u = \tilde{u}U, \quad v = \tilde{v}U, \quad T = \tilde{T}f^{-1},$$
$$H_x = \tilde{H}_{\tilde{x}}\frac{\Delta H}{W} = \tilde{H}_{\tilde{x}}\frac{\Delta\tilde{H}}{\tilde{W}}\frac{H_+}{R_d}, \tag{5}$$

where the tilde variables are the nondimensionalized ones.

The parameters governing the problem are as follows: the Rossby (or Froude) number, $\epsilon = U/fR_d$, the relative elevation of the free surface, $\lambda = \Delta\eta/H_+$, and the ratio of the relative depth change due to the escarpment to the half-width of the slope, $\sigma = \Delta\tilde{H}/\tilde{W}$. Under the assumption $\lambda \sim \epsilon$ (which is necessary in order to get the geostrophic equilibrium in the leading order in ϵ), the nondimensional equations become, omitting the tildes,

$$u_t + \epsilon(uu_x + vu_y) - fv = -\eta_x, \tag{6}$$

$$v_t + \epsilon(uv_x + vv_y) + fu = -\eta_y, \tag{7}$$

$$\lambda\eta_t + \epsilon H(u_x + v_y) + \epsilon\sigma H_x u + \lambda\epsilon[(u\eta)_x + (v\eta)_y] = 0. \tag{8}$$

This nondimensional form of the equations is used in the numerical simulations.

As the initial condition, we take a perturbation of the free surface in a form of step function along a straight line perpendicular to the escarpment. The perturbation is positive in the negative y domain and null elsewhere. This initial configuration is purposely chosen to be the same as the one used by Allen,[3] in order to benchmark our simulations. For fully nonlinear numerical simulations of this problem we apply the high-resolution shock-capturing finite-volume technique proposed in Ref. 8. The method was first used and extensively tested in the front adjustment problem in Ref. 7. For a complete description of the procedure and discussion of its properties, see Ref. 9.

We briefly review the main ingredients of the method. The shallow water equations in the flux-form are discretized on a regular grid within the framework of the finite-volume approach. The finite-volume scheme is then prescribed by the choice of the numerical flux function and the treatment of the remaining source terms associated with the Coriolis force. At each time step and in each direction, the Coriolis terms are reformulated following the apparent topography method first introduced in Ref. 7. The numerical flux function is associated with a relaxation solver adapted to treat topography as proposed in Ref. 14. The choice of the numerical flux function allows us to compute solutions of the shallow water equations even in the case of vanishing depth. The numerical scheme is inviscid, the numerical dissipation being extremely small except for the shock locations. The variable time step is used in order to verify the Courant–Friedrichs–Lewy (CFL) condition. The numerical simulations discussed below are obtained with a typical resolution $\Delta x, \Delta y \sim 0.1R_d$. The computations take a few hours on a personal computer at this resolution. For steep topography, the resolution was correspondingly increased. In order to avoid the returns of IGW emitted during adjustment, the sponge layers are used at the boundaries (except for the coast, if present; see below).

III. EXPECTED SCENARIO OF THE ADJUSTMENT OF THE PRESSURE FRONT AND FURTHER QUESTIONS

From the knowledge of the previous results on nonlinear adjustment of the pressure front without topography,[4] of the numerical results on linear adjustment with topography,[3] and of the experimental and theoretical results with step-function escarpments,[1,2] we can expect the following processes to take place: on the shortest time scales, the IGW are to be emitted, to propagate away from the initial discontinuity, and to break at sufficient nonlinearities. Their propagation and breaking will be modified, with respect to the flat bottom situation, due to the fact that the phase speed of IGW varies with varying depth of the fluid. A jet will form along the initial discontinuity, in order to balance the pressure gradient. On longer time scales, topographically trapped waves (called either double Kelvin waves or topographic Rossby waves) should arise at the intersection of the initial front with the slope. The trapped waves propagate along the escarpment with shallower water on their right in the northern hemisphere.[15] The long trapped waves will form a tongue propagating in this way, which will distort the jet and make it follow the contour of the nose of the tongue. The group velocities of short and long topographic waves are opposite (see below). A packet of short waves will also be emitted and will propagate in the opposite direction with respect to the tongue, but with much slower velocity and, presumably, carrying not much energy, as in the simulations by Allen.[3]

Once these predictions for initial stages of adjustment are checked, the main questions that the fully nonlinear numerical simulation should answer are the following:

- How is the propagation and breaking of IGW modified by topography?
- What is the long time evolution of the trapped waves?
- What are the mixing and transport properties of the adjustment process?

IV. THE RESULTS OF NUMERICAL SIMULATIONS FOR THE ADJUSTMENT OF THE FRONT OVER TOPOGRAPHY FAR FROM THE COAST

A. Small nonlinearity

In order to benchmark our simulations and compare them with those in Ref. 3, we start with a small nonlinearity $(\lambda=\Delta\eta/H_+=0.1)$.[16] We choose the width of the slope equal to five Rossby deformation radii for the simulations in this and the following sections, and $H_+=2H_-$. We will discuss the effects of varying the parameters of the slope in Sec. IV C. In all of the figures below, the spatial coordinates are measured in R_d, so that $W=2.5R_d$, and the time is measured in f^{-1}. Figure 2 gives the time evolution of the free-surface elevation, the initial state being at rest, $u(x,y,0)=v(x,y,0)=0$. A zoom of the last frame in Fig. 2 (at $t=150$) with superimposed velocity field (arrows), and the corresponding three-dimensional snapshot of the free-surface elevation, are given in Fig. 3. Emission of the IGW takes place at the initial stages of the evolution. The IGW fronts originating from the

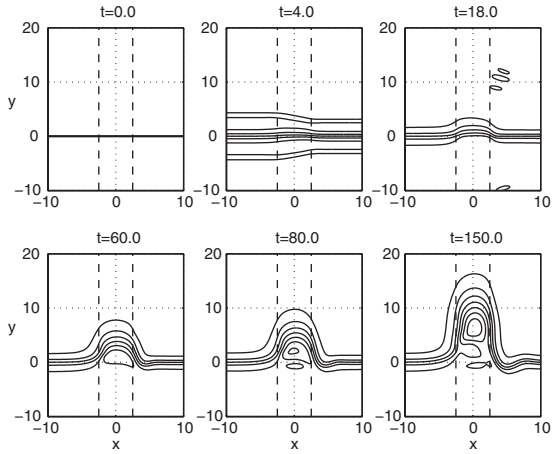

FIG. 2. The time evolution of the free-surface elevation in the (x,y) plane. The initial perturbation is equal to $+\Delta\eta$ in the lower part of the domain $(y<0)$ and zero in the upper part $(y>0)$. The edges of the slope are marked with dashed lines, $\lambda=0.1$; the difference between the adjacent isolines of the free-surface height (isobars) is 0.02. The size of the calculation domain in the y direction is much bigger than the displayed domain.

initial discontinuity start bending (cf. the second frame of Fig. 2). The wave packets of IGW, apparently emitted at the location of maximum curvature of the primary IGW fronts, are observed (cf. the third frame of Fig. 2). The IGW fronts will be discussed below in Sec. IV D 2. The topographic Rossby waves in the form of localized height extrema along the slope that form a tongue appear at the later stages. The figure shows clearly that the topographic waves are close to the geostrophic balance (flow parallel to the isobars). They are, thus, a part of the slow balanced motion, like the "ordinary" Rossby waves on the beta-plane. The dispersion relation for the topographic Rossby waves[17] is also similar to that of ordinary Rossby waves;[11] see Fig. 4. Our simulations are, thus, in a good qualitative agreement with the results of Ref. 3: we confirm the formation of an anticyclonic vorticity region at the slope, the propagation of a tongue of fluid along the escarpment keeping the shallow water on its right and tending to separate the flows on the two sides of the slope. Apart from the jet going around the tongue, only a very small amount of fluid is crossing the escarpment at the location of the initial discontinuity.

In order to better visualize the behavior of the topographic wave packet, we present the time evolution of the fluid depth at the center of the slope $(x=0)$ as a function of y in Fig. 5. The amplitude of the topographic waves grows during approximately ten of inertial periods and then saturates, while secondary extrema are formed. It should be noticed that the amplitude of the first maximum grows higher than the initial perturbation (the maximum height is about 140% of the initial height). The topographic waves propagate without visible distortion, as seen in the figure.

To push the comparison further, we measured the speed of propagation along the escarpment of both the leading edge of the tongue and of the principal height maximum. The former is obtained, as in Ref. 3, by following the level at half-height of the initial perturbation, i.e., at $h=1.05$ in Fig. 5. We thus get

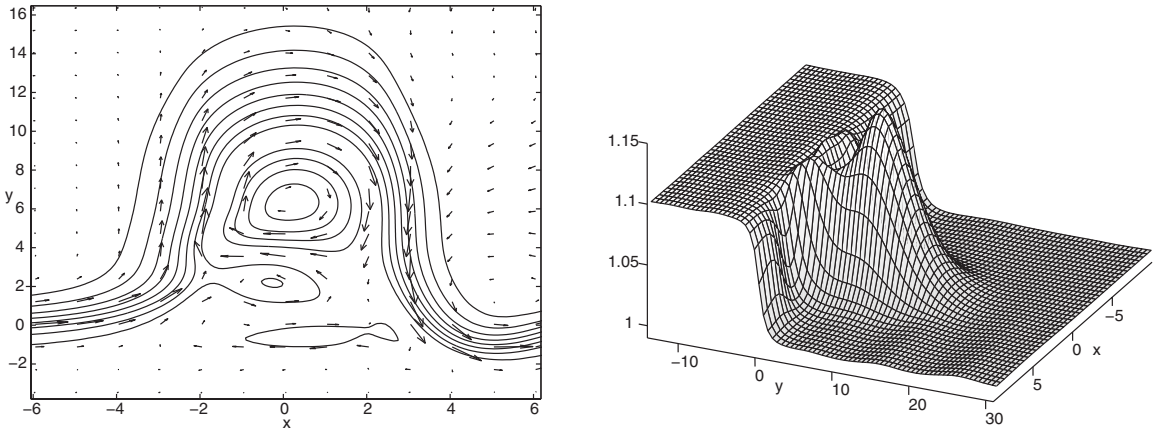

FIG. 3. Zoom of the late ($t=150$) stage of the evolution of the free-surface elevation with superimposed velocity field (arrows) (left panel); and the 3D view of the height field at the same time (right panel). Same experiment as in Fig. 2.

$$v_{\text{edge}} \approx 0.08, \quad v_{\text{peak}} \approx 0.06 \tag{9}$$

in terms of $\sqrt{gH_+}$. The obtained value of v_{edge} is substantially larger than the value following from Fig. 8 in Ref. 3 for the same escarpment.

The difference between v_{edge} and v_{peak} means that the topographic wave packet is subject to dispersion. The typical wavelength of the topographic waves formed in the adjustment process may be extracted from the simulations. It allows us to estimate the phase and group velocity of the corresponding *linear* wave with the help of Fig. 4. For instance, an estimate of the wavelength as a distance between the two maxima of the height field, cf. Fig. 5, gives $k \approx 0.92$, $c_g \approx 0.019$, and $c_\phi \approx 0.056$. However, these figures change significantly if twice the width of the negative curvature region of the principal height peak is taken as typical wavelength: $k \approx 0.56$, $c_g \approx 0.048$, and $c_\phi \approx 0.072$. Thus, the identification of the measured propagation speed with the phase or group velocity of the linear waves cannot be done in a clearcut way. We therefore measured the dispersive effects directly by following the widening of the principal peak in h during the evolution. We thus obtain a widening of about 10% in $100f^{-1}$, which is very low comparing with the expected widening due to the difference between the phase and the group velocity for both estimates given above.

The across-slope profile of the first maximum of the fluid height is close to the profile of the fundamental mode given by the linear theory, but some differences appear while superimposing them, as illustrated in Fig. 6. The linear modes shown in Fig. 6, as well as the dispersion curves above, are obtained by a straightforward numerical resolution of the linear eigenvalue problem for the trapped modes by the shooting method. Figure 4 agrees with the dispersion obtained in Ref. 3 for the same escarpment, e.g., zero c_g is at $k=1.3$. Note that in agreement with Ref. 11, the maximum of the curves is shifted toward the shallower side of the slope.

The above observations allow us to suggest that the effects of nonlinearity manifest themselves already at small λ and play a role in the coherence of the observed wave structure. We show in the Appendix that modulated topographic waves, at small nonlinearities, obey the Korteweg–de Vries equation for a given across-slope mode, and thus can form solitons. Although our initial perturbation does not project

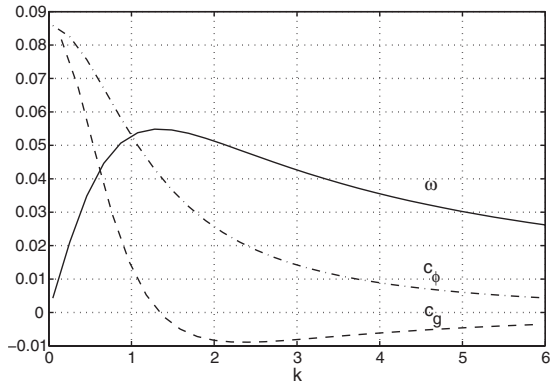

FIG. 4. Dispersion curve, phase (c_Φ) and group (c_g) velocities of the topographic Rossby waves, obtained by a straightforward numerical resolution of the linear eigenproblem for the topographic Rossby waves by the shooting method (cf. Ref. 11). The along-slope wavenumber is nondimensionalized by R_d, and the frequency ω is nondimensionalized by the inertial frequency f.

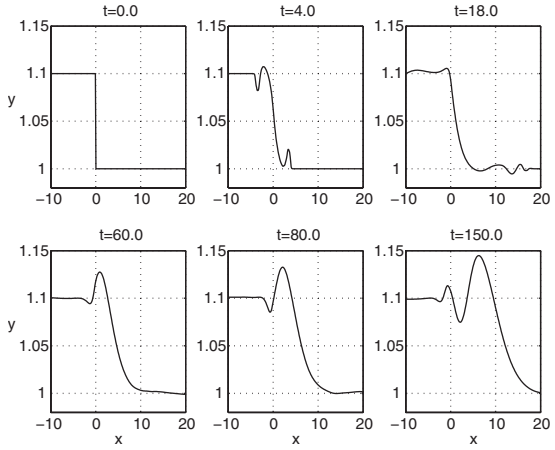

FIG. 5. Time evolution of the fluid height profile at the center of the slope ($x=0$) along the y axis. Same experiment as in Fig. 2, $\lambda=0.1$.

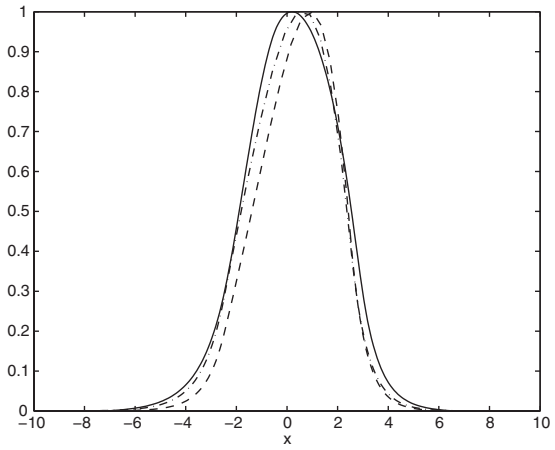

FIG. 6. The nondimensional profiles of the fundamental modes of the linear theory corresponding to $k=0.92$ (dashed line) and to $k=0.56$ (dash-dotted line) vs the section of the first pressure maximum in the numerical simulation of Fig. 2 (solid line) at time $t=150$ as functions of nondimensional x.

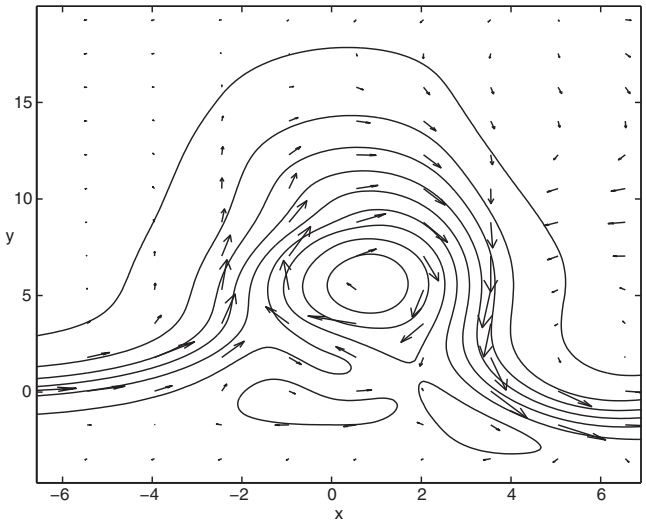

FIG. 8. Same as in the left panel of Fig. 3 but at $\lambda=0.3$. The isobars from $h=1.02$ up at step 0.05 are displayed.

onto a single mode, the observed behavior of the subsequent pressure maxima is qualitatively consistent with that of a soliton train.

B. Strong nonlinearity

We now focus on the same process but at a larger initial nonlinearity $\lambda=0.3$. Figure 7 shows the nonlinear evolution of the free-surface elevation and Fig. 8 gives a zoom of the last frame at $t=150$ with superimposed velocity field (arrows). The scenario of the adjustment is qualitatively the same as at $\lambda=0.1$. The topographic waves propagate without distortion, and the amplitude of the first maximum again grows higher than the initial height of the perturbation (maximum height is about 130% the initial height; see Fig. 9). The measured speeds of the edge of the tongue and that of the principal height maximum are close to those at smaller nonlinearity,

$$v_{\text{edge}} \approx 0.08, \quad v_{\text{peak}} \approx 0.05. \tag{10}$$

The left panel of Fig. 8 shows that the flow is again close to the geostrophic balance but it is less equilibrated on the shallow side.

There are, however, some differences between the two cases. The emission of inertia-gravity waves takes place during a longer period of time (about $30f^{-1}$). The secondary extrema of the height field are formed later: at $t=200$ there are three maxima and two minima in the profile of h at small nonlinearity, and only two maxima and two minima at strong nonlinearity (not shown).

The estimates of the typical wavenumber, group, and phase velocities based on the same criteria as in the preceding section give, respectively, $k\approx 0.98$, $c_g\approx 0.015$, $c_\phi\approx 0.054$ and $k\approx 0.73$, $c_g\approx 0.033$, $c_\phi\approx 0.064$. The widening of the principal pressure peak during $100f^{-1}$ is again $\sim .1$, and is much slower than that given by the linear dispersion. The comparison of the profiles of linear modes with the mea-

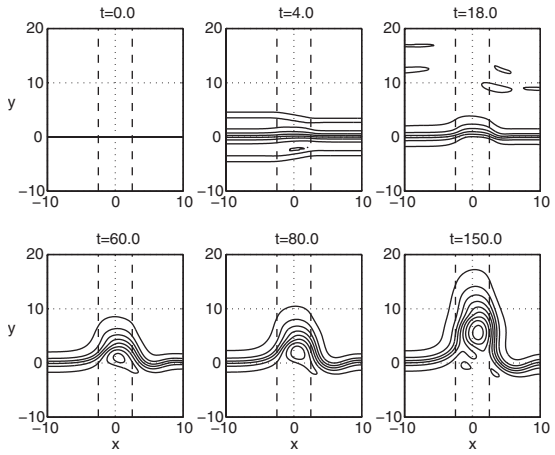

FIG. 7. Same as in Fig. 2, but at $\lambda=0.3$. The difference between the adjacent isolines of the free-surface height (isobars) is 0.05.

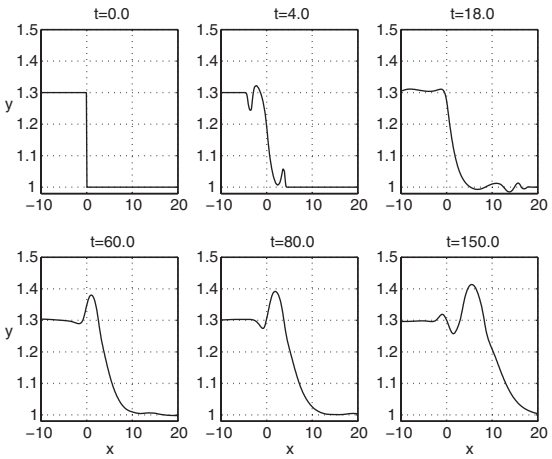

FIG. 9. Same as in Fig. 5 but at $\lambda=0.3$.

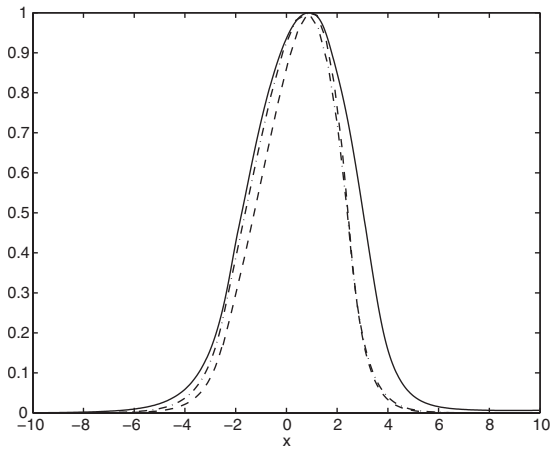

FIG. 10. The nondimensional profiles of the fundamental modes of the linear theory corresponding to $k=0.98$ (dashed line) and to $k=0.73$ (dash-dotted line) vs the section of the first pressure maximum in the numerical simulation of Fig. 7 (solid line) at time $t=150$, as functions of nondimensional x.

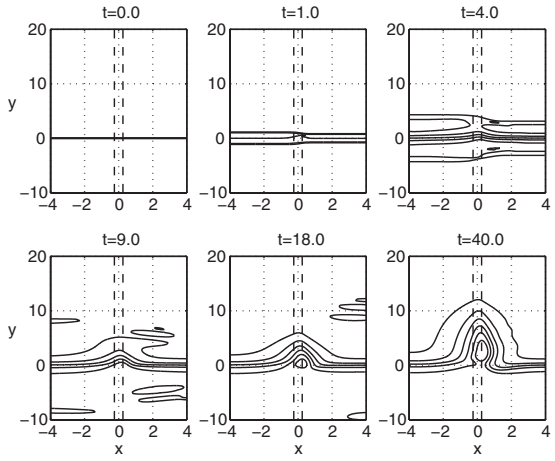

FIG. 11. The time evolution of the free-surface elevation in the (x,y) plane. The initial perturbation is equal to $+\Delta\eta$ in the lower part of the domain $(y<0)$ and zero in the upper part $(y>0)$. The edges of the slope are marked with dashed lines $(W=0.25)$, $\lambda=0.1$, and the height difference between the adjacent isolines of the free-surface height is 0.02. The length of the calculation domain in the y direction is much bigger than the displayed domain.

sured profile of the main pressure peak presented in Fig. 10 shows some differences, e.g., the widening of the nonlinear profile.

Globally, the simulations at $\lambda=0.3$ confirm the coherent-structure character of the topographic wave pattern formed during adjustment. This character is strengthened even more by its stirring properties displayed in Sec. IV D.

C. Steep topography

In this section, we briefly describe how the previous results are modified for the steep topography. One of the motivations is the comparison with the theoretical and experimental results obtained in Refs. 1 and 2 for an "infinitely steep," i.e., step-function profile of the escarpment. The numerical code we use, by construction (cf. the explicit expressions for numerical fluxes in Ref. 7), cannot treat the step-function topography. Hence, the only way to model the abrupt topography is to take a steep escarpment. This means, in turn, that spatial resolution across escarpment should be increased. We thus consider a slope of a half-width, $W=0.25R_d$, i.e., ten times steeper than in the previous subsections, with the same ratio of depths $H_-=0.5H_+$. We start from a weakly nonlinear pressure front with $\lambda=0.1$. The evolution of the free surface is presented in Fig. 11. We stopped the simulation at $t=40$ as it is getting increasingly costly to go further in time because of the increased resolution. The overall scenario of adjustment is qualitatively the same as in the case of gentle topography, with the following main differences:

(1) The velocity of the topographic waves is much slower.
(2) The tongue is less confined to the escarpment, i.e., it spreads outside the slope.
(3) The peak is shifted toward the top of the slope.

A zoom of the last frame in Fig. 11 with superimposed velocity vectors is shown in Fig. 12, with the three-dimensional view of this same stage. We see that the peak height exceeds the initial maximum height and that the flow is approximately in geostrophic balance at the deep side, but at the shallow side we notice significant departures from the geostrophic balance, probably due to relatively short integration time. Note also the presence of the small-amplitude IGW in Fig. 12, which are deforming the isobars. The speed of the propagation of the tongue is much faster, which is consistent with the increase of the phase velocity of the trapped waves with increasing slope; cf. Ref. 11. Nevertheless, the velocity of the main pressure peak is of the same order of magnitude as in the case of gentle topography,

$$v_{\text{edge}} \approx 0.2, \quad v_{\text{peak}} \approx 0.08. \tag{11}$$

Qualitatively, these results are consistent with the linear analysis of Ref. 2 with a notable exception of the observed dissymmetry with respect to the axis of the slope.

D. Transport, stirring, and mixing during the adjustment of the pressure front

1. Anomalous transport due to nonlinear topographic waves

In order to study the transport and stirring properties of the adjustment process, we add a new variable, the density of a passive tracer, to the previous runs, and follow its evolution.[18] We use the same method, well adapted for the finite-volume code, and the same mode of visualization of the tracer as in Ref. 13, i.e., we follow the evolution of the isopycnals of the tracer distribution initially linear in one of the coordinates. We show in the figures below the simultaneous evolution of the pair of tracers, distributed initially linearly in x and in y, respectively. Thus, each intersection of the isopycnals represents a fluid particle.

As was already mentioned, we are motivated by similar studies for the equatorial adjustment,[12,13] where it was shown that the waveguide modes at sufficient nonlinearities may form coherent structures (modons of equatorial Rossby

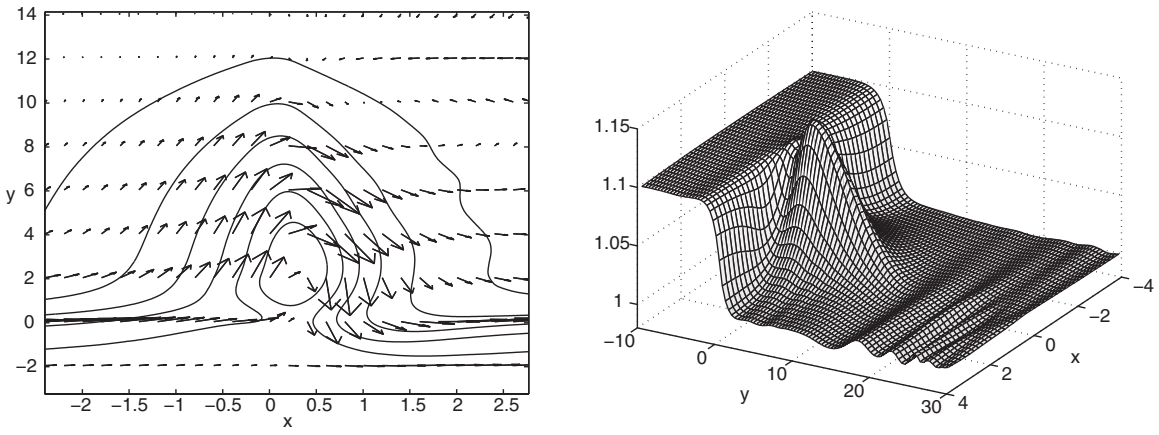

FIG. 12. The late ($t=40$) stage of the evolution of the free-surface elevation with superimposed velocity field (arrows) (left panel); and the corresponding 3D view of the height field (right panel). Same experiment as in Fig. 11. Note that the x scale here is different with respect to Figs. 2 and 7.

waves in that case) trapping fluid and carrying it along the waveguide. We show here that although the spatial structure of the waveguide modes in the present case is not the same (they are monopolar, and not dipolar, as at the equator), the same phenomenon takes place.

Figure 13 gives the spatio-temporal evolution of the tracer field during the adjustment of the front with $\lambda=0.1$ over the gentle topography $W=2.5R_d$. In the last frame ($t=150$), we observe a formation of a recirculation pattern, with subsequent trapping of the fluid. This is a "dispersive breaking" phenomenon, as it was called in Ref. 13. At larger nonlinearity, trapping appears earlier, as we can see in Fig. 14, where the nonlinearity is $\lambda=0.3$. The topographic waves are again trapping fluid and carrying it along the escarpment.

2. Wave-breaking as an indicator of mixing

As was already mentioned in the Introduction, our numerical model is essentially nondissipative except for the shock locations.[7] The total energy is conserved during the simulations, apart from the events of wave-breaking. We show in Fig. 15 the time evolution of the total energy loss in the flow in the frontal adjustment process. The energy loss is pronounced during the initial stages of evolution (several inertial periods) where the strong gradients (due to initial conditions, and to the secondary shock formation; see below) are present. The secondary peak of the energy loss at $t\sim 6$ is correlated with the appearance of the strongly curved region at the emitted wave-front; see Fig. 16. The energy loss is very low during the rest of the simulation, which amounts to the overall loss of energy of the order of one per thousand.

Due to the difference in the phase speeds of waves on the left and on the right of the escarpment (IGW propagating faster in deeper fluid), the wave-fronts of the IGW emitted at the initial stage of adjustment should bend. This is a novel aspect of the dam-break problem in the presence of topography, which should affect the wave-breaking accompanying the propagation of such wave-fronts.[4,7] By monitoring the local dissipation rates, we can identify the wave-breaking

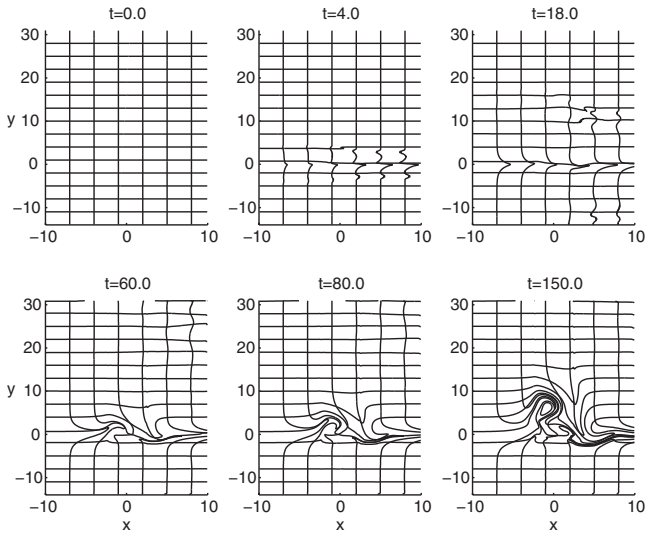

FIG. 13. Time evolution of the tracer field at $\lambda=0.1$ and $W=2.5R_d$. The isopycnals of a pair of passive tracers with initial distributions linear in x and y, respectively, are shown in subsequent times. Tracers are advected by the velocity field corresponding to the simulation of Fig. 2.

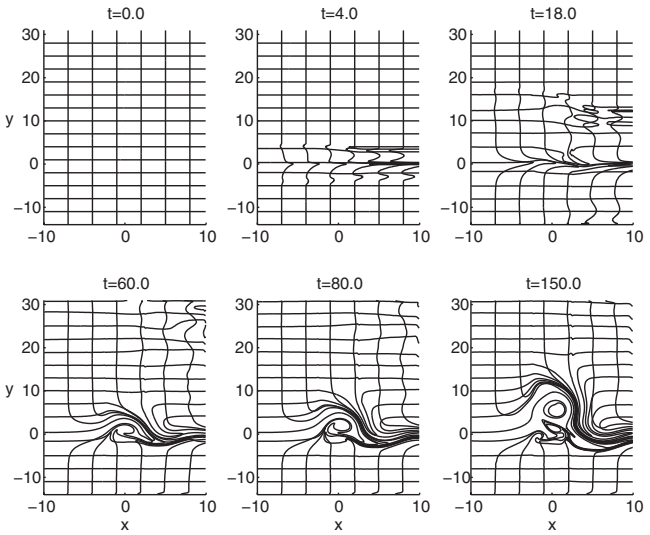

FIG. 14. Time evolution of the tracer field at nonlinearity $\lambda=0.3$ and $W=2.5R_d$. See the caption of Fig. 13.

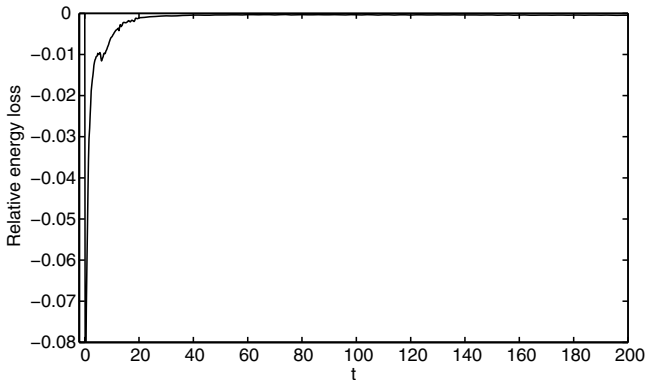

FIG. 15. Time evolution of the energy loss due to numerical dissipation of the flow at $\lambda=0.3$. The relative energy loss per unit time $\Delta E/E_0\Delta t$ is calculated as deviation from the energy balance in each calculation cell, integrated over the whole calculation domain and normalized by the total initial energy.

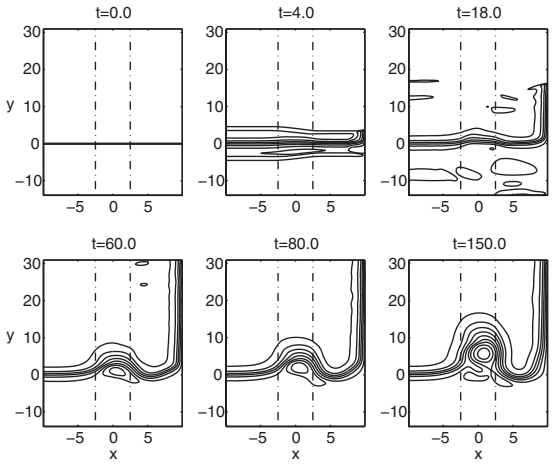

FIG. 17. Time evolution of the free-surface elevation in the (x,y) plane, at $\lambda=0.3$. The solid wall is on the right side.

zones. The evolution of the local dissipation rate in the calculation domain at the initial stages of the simulation with $\lambda=0.3$ is shown in Fig. 16. The dissipation rate is calculated as the deviation from the energy conservation in each computation cell. The zones where the dissipation is prominent are located first at the two wave-fronts propagating from the initial discontinuity in both along-slope directions. After several of the inertial periods, the maximum of dissipation is localized at the specific zones of the IGW wave-fronts propagating at the shallow side of the escarpment. As seen from the figures, the IGW wave-front intensity is decreased, except for these precise locations that continue to propagate as localized wave-packets at an angle that is the same in simulations with different front intensities.

Obviously the highly idealized model cannot pretend to correctly represent the dissipative phenomena in the real flow (recall that the typical resolution is 0.1 R_d in the simulations above). However, it gives a good first guess about locations of enhanced dissipation and hence mixing in the real flow in similar configurations.

V. THE ROLE OF THE COAST

In the previous simulations, the escarpment was situated in the "open ocean." Let us briefly comment on the new effects introduced by an adjacent coast line. The effects of the coast perpendicular to the escarpment were discussed by Gill, Davey, Johnson, and Linden[1] and Allen.[3] We repeated our simulations with $W=2.5R_d$ by placing a rigid wall parallel to the escarpment at $x=10$ at the shallow side in order to model a "continental shelf" configuration. The results for the evolution of the height field, the dissipation, and the profile of the height field along the $x=9$ section are given in Figs. 17–19 , respectively.

The main new element introduced by the coast is the propagation of the boundary Kelvin wave front along it. Due to the fact that the boundary Kelvin waves are dispersionless, they break (cf. Ref. 19) and form the mixing zones. The

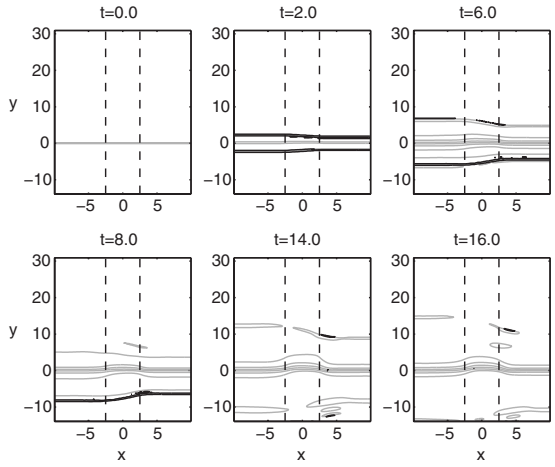

FIG. 16. Time evolution of the dissipation rate (black contours corresponding to the threshold of 2×10^{-5} in nondimensionalized energy flux unit) superimposed on the surface elevation (gray contours at $\Delta h=0.05$ interval) in the (x,y) plane, at $\lambda=0.3$.

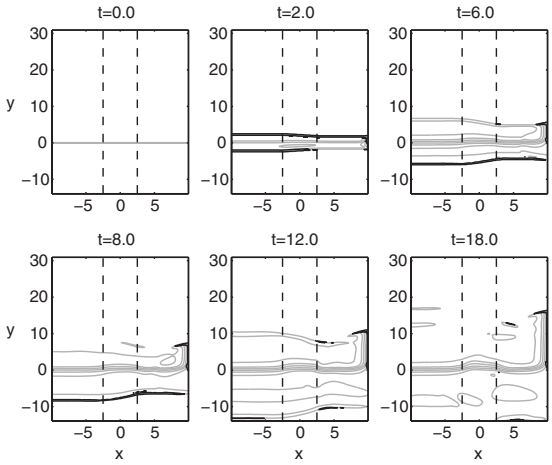

FIG. 18. Joint evolution of the dissipation rate (black contours) and the free-surface elevation (gray contours) in the (x,y) plane, at $\lambda=0.3$.

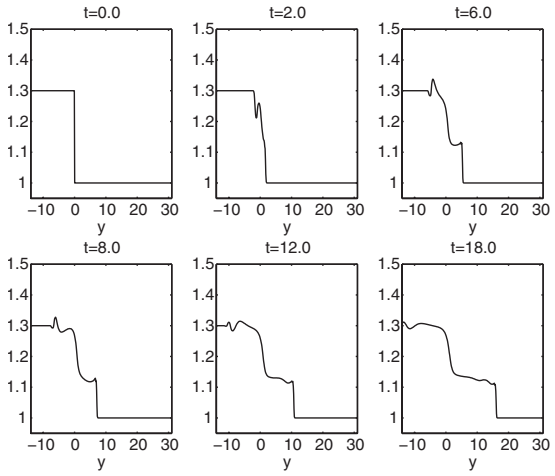

FIG. 19. Time evolution of the free-surface elevation at $x=9$ (close to the wall), at $\lambda=0.3$.

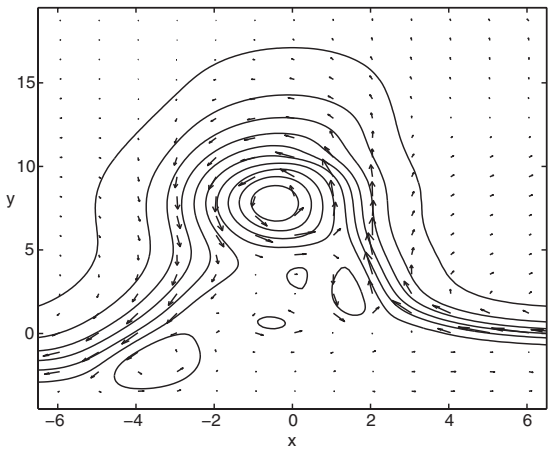

FIG. 20. Same as in Fig. 8 but for the reversed initial anomaly. Isobars from $h=0.98$ down at step 0.05 are displayed.

details of the Kelvin front formation are given in Fig. 19. Another phenomenon related to the Kelvin front propagation is a secondary wave emission behind the front well-distinguishable in the pressure contours in Fig. 18. It is similar to that observed for equatorial Kelvin fronts[20,12] and has the same explanation. Namely, the nonlinear Kelvin waves having phase speed higher than the linear one may be in a direct resonance with the IGW.

VI. CONCLUSIONS AND DISCUSSION

We have performed detailed fully nonlinear numerical simulations of the classical problem of the adjustment of a pressure front over topography. We confirmed the results of earlier investigations that were performed previously in the linear regime and found new essentially nonlinear phenomena. The most important of them, in what concerns dynamics, is excitation of finite-amplitude topographic waves propagating essentially without change of form for long times, and resembling the soliton trains known from the theory of the KdV equation. Nevertheless, the quantitative check of the soliton hypothesis is yet to be done. In what concerns transport and mixing, the most characteristic features are (i) formation of recirculation regions in the cores of topographic "solitons" with subsequent anomalous tracer transport along the topography, and (ii) appearance of specific mixing zones related to the propagation of IGW, or of the boundary Kelvin waves in the presence of the coast, emitted during the early stages of adjustment.

Therefore, the geostrophic adjustment in the presence of the topographic waveguide is specific and resembles that at the equator, as part of the initial perturbation projects onto the waveguide modes. These waveguide modes form coherent structures providing the anomalous transport along the waveguide. The waveguide modes belong to the balanced part of the motion, as we confirm by direct calculations. They evolve much slower than unbalanced IGW, which evacuate the excess of energy at the early stages of the adjustment process. The IGW are, however, also influenced by topography, which leads to the enhancement of dissipation/mixing in specific locations.

It should be mentioned that fully nonlinear numerical simulations of the interaction of jets with topography using the rigid-lid configuration are known in the literature.[21] The rigid-lid approximation corresponds formally to $R_d \to \infty$, which physically means that all typical scales, including the scale of the slope, are much smaller than the deformation radius. The steep topography case in Sec. IV C above is the only one approaching this regime in the present study (such scales are largely subgrid in the gentle slope case). However, our simulations reveal the formation of the coherent structures of the scale still much larger than the width of the slope, which was not the case in the corresponding cases in Ref. 21. The dipolar structures corresponding to the higher topographic modes were typically observed in Ref. 21, while in our simulations the monopolar ones are dominating, although higher modes can appear on the late stages as suggested by the gentle-slope simulations (cf., e.g., Fig. 8). It probably means that even with steep topographies, the rigid-lid regime is hard to reach in the full rotating shallow water model. This is also true for the adjustment with the reversed jet (initial pressure anomaly of opposite sign), which was also studied in Ref. 21. We present in Fig. 20 the late stage of the evolution for strong nonlinearity $\lambda=0.3$ in this case, to be compared with Fig. 8. The topology of the isobars is globally the same, although it corresponds to a trough in Fig. 20 and to an elevation in Fig. 8, with respect to the nonperturbed fluid surface at rest. Some asymmetry, however, is observed in what concerns the intensity of the resulting balanced vortex (more intense in Fig. 20) and its position (at the shallower side of the slope for the cyclonic vortex, Fig. 20, and at the deeper side for the anticyclonic vortex, Fig. 8). Being more intense, the vortex/pressure extremum propagates faster in Fig. 20, although the tip of the tongue has practically the same velocity in both cases.

APPENDIX: KdV SOLITONS OF MODULATED TOPOGRAPHIC WAVES

Consider the shallow-water equations with topography (1)–(3) on the f plane.

We use a slightly different nondimensionalization with respect to Eqs. (4) and (5) for the horizontal scale, the vertical scale, and the velocity, because we want to allow for different scales in the two horizontal directions. Using the half-width of the slope W as a typical horizontal scale in the x direction, L, a typical horizontal scale in the y direction with the corresponding aspect ratio parameter $\delta = W/L$ supposed to be small, the mean depth of the fluid at rest $\bar{H} = H_+ + H_-/2$ as a vertical scale, and δU and U for the zonal and meridional velocity, respectively, we nondimensionalize the dependent and independent variables as follows:

$$x = \tilde{x}W, \quad y = \tilde{y}L, \quad H = \tilde{H}\bar{H}, \quad \Delta H = \Delta\tilde{H}\bar{H}, \quad \eta = \tilde{\eta}\Delta\eta, \tag{A1}$$

$$u = \tilde{u}\delta U, \quad v = \tilde{v}U, \tag{A2}$$

$$T = \tilde{T}f^{-1}, \quad H_x = \tilde{H}_{\tilde{x}}\frac{\Delta H}{W} = \tilde{H}_{\tilde{x}}\Delta\tilde{H}\frac{\bar{H}}{W},$$

where the tilde variables are the nondimensionalized ones. The parameters governing the problem, thus, are as follows: the Rossby number $\epsilon = U/fW$, the relative elevation of the free surface $\lambda = \Delta\eta/\bar{H}$, the Burger number $\gamma = (R_d/W)^2$, where the Rossby deformation radius is defined as $R_d = \sqrt{g\bar{H}/f^2}$, and the relative depth change due to the escarpment, $\sigma = \Delta\tilde{H}$.

We get the following nondimensionalized set of equations:

$$\delta u_t + \epsilon\delta^2(uu_x + vu_y) - v = -\frac{\lambda\gamma}{\epsilon}\eta_x, \tag{A3}$$

$$v_t + \epsilon\delta(uv_x + vv_y) + \delta u = -\delta\frac{\lambda\gamma}{\epsilon}\eta_y, \tag{A4}$$

$$\lambda\eta_t + \epsilon\delta H(u_x + v_y) + \epsilon\delta\sigma H_x u + \lambda\epsilon\delta[(u\eta)_x + (v\eta)_y] = 0. \tag{A5}$$

We are interested in slow motions close to the geostrophic equilibrium. The latter is achieved at the leading order by the following choice of parameters: $\lambda\gamma/\epsilon \sim 1$, which is standard in the quasigeostrophic dynamics. The filtering of the fast inertia-gravity waves is achieved by using the hierarchy of the slow time scales, $t_n = \delta^n t$, and supposing that all the fields are slow, i.e., do not depend on the fast time scale t_0. Finally, the nonlinearity, as well as the Rossby number, are supposed to be small and we choose the following relation among the small parameters: $\lambda \sim \epsilon \sim \delta^2$, $\gamma \sim 1$, meaning that the width of the escarpment is of the order of the Rossby radius. We thus get, omitting the numerical factors of order 1,

$$\delta^2(u_{t_1} + \delta u_{t_2} + \delta^2 u_{t_3} + \cdots) + \delta^4(uu_x + vu_y) - v = -\eta_x, \tag{A6}$$

$$(v_{t_1} + \delta v_{t_2} + \delta^2 v_{t_3} + \cdots) + \delta^2(uv_x + vv_y) + u = -\eta_y, \tag{A7}$$

$$(\eta_{t_1} + \delta\eta_{t_2} + \delta^2\eta_{t_3} + \cdots) + Hu_x + Hv_y + \sigma H_x u + \delta^2[(u\eta)_x + (v\eta)_y] = 0. \tag{A8}$$

The last hypothesis consists in supposing the order 1 depth change across the escarpment, $\sigma \sim 1$. All fields are then expanded in asymptotic series in δ,

$$u = u^{(0)} + \delta u^{(1)} + \delta^2 u^{(2)} + \cdots,$$

$$v = v^{(0)} + \delta v^{(1)} + \delta^2 v^{(2)} + \cdots,$$

$$\eta = \eta^{(0)} + \delta\eta^{(1)} + \delta^2\eta^{(2)} + \cdots.$$

At the lowest order we get

$$v^{(0)} = \eta_x^{(0)}, \tag{A9}$$

$$v_{t_1}^{(0)} + u^{(0)} = -\eta_y^{(0)}, \tag{A10}$$

$$\eta_{t_1}^{(0)} + Hu_x^{(0)} + Hv_y^{(0)} + H_x u^{(0)} = 0, \tag{A11}$$

which is equivalent to a single equation for $\eta^{(0)}$,

$$\partial_{t_1}[H\eta_{xx}^{(0)} + H_x\eta_x^{(0)} - \eta^{(0)}] + H_x\eta_y^{(0)} = 0. \tag{A12}$$

Looking for a propagating in y solution with a given structure in x,

$$\eta^{(0)} = F^{(0)}(x)\Phi^{(0)}(ky - \omega t_1, t_2, t_3, \ldots) \tag{A13}$$

we get the following equation for the across-escarpment structure functions,

$$[HF_x^{(0)}]_x - F^{(0)}\left(1 + \frac{k}{\omega}H_x\right) = 0. \tag{A14}$$

The solutions of this equation in the case of linear topography are expressed in terms of the modified Bessel function of the first kind and of the second kind.

Due to the assumed scaling, this equation is the long-wave low-frequency limit of the equation for the linear modes obtained by the straightforward linearization about the rest state of Eqs. (1)–(3), and used earlier to get Fig. 4. It is easy to see that in order to get nontrivial eigenmodes $F_n^{(0)}(x)$ with eigenfrequencies ω_n, it is necessary that $(1 + k/\omega H_x)$ changes sign. Thus, for monotonous escarpment-like topography, the well-known unique direction of propagation of the topographic waves which keep shallower water on their right in the Northern hemisphere[15] follows.

Proceeding to the higher orders in δ will give, as usual in the asymptotic expansions method, a series of inhomogeneous problems for higher corrections $\eta^{(i)}, i = 1, 2, ..$ with the right-hand side (r.h.s.) depending on the previous-order fields. Again, according to the standard rules, the solutions of these problems may be obtained by removing the resonances on the r.h.s., i.e., imposing the orthogonality condition and

introducing dependence on slower times. This gives the nonlinear evolution equation for $\eta^{(0)}$. Proceeding in this way, it is easy to see that it is sufficient to require that there is no t_2 dependence in the zero-order fields to get rid of the resonances at the first order in δ. At the order δ^2, we have

$$u^{(0)}_{t_1} - v^{(2)} = -\eta^{(2)}_x, \tag{A15}$$

$$v^{(2)}_{t_1} + v^{(0)}_{t_3} + u^{(0)}v^{(0)}_x + v^{(0)}v^{(0)}_y + u^{(2)} = -\eta^{(2)}_y, \tag{A16}$$

$$\eta^{(2)}_{t_1} + \eta^{(0)}_{t_3} + H[u^{(2)}_x + v^{(2)}_y] + u^{(2)}H_x + [u^{(0)}\eta^{(0)}]_x + [v^{(0)}\eta^{(0)}]_y = 0. \tag{A17}$$

By expressing the velocity field in terms of the free-surface elevation,

$$v^{(2)} = \eta^{(2)}_x - \eta^{(0)}_{yt_1} - \eta^{(0)}_{xt_1t_1}, \tag{A18}$$

$$u^{(2)} = -\eta^{(2)}_y - \eta^{(2)}_{xt_1} + \eta^{(0)}_{yt_1t_1} + \eta^{(0)}_{xt_1t_1t_1} - \eta^{(0)}_{xt_3} - \eta^{(0)}_x\eta^{(0)}_{xy} + (\eta^{(0)}_y + \eta^{(0)}_{xt_1})\eta^{(0)}_{xx}, \tag{A19}$$

we get

$$\begin{aligned} -H\eta^{(2)}_{xxt_1} - H_x[\eta^{(2)}_{xt_1} + \eta^{(2)}_y] + \eta^{(2)}_{t_1} &= -\eta^{(0)}_{t_3} - H[\eta^{(0)}_{xyt_1t_1} + \eta^{(0)}_{xxt_1t_1t_1} - \eta^{(0)}_{xxt_3} - \eta^{(0)}_x\eta^{(0)}_{xxy} \\ &+ \eta^{(0)}_{xxt_1}\eta^{(0)}_{xx} + \eta^{(0)}_y\eta^{(0)}_{xxx} + \eta^{(0)}_{xt_1}\eta^{(0)}_{xxx} - \eta^{(0)}_{yyt_1} - \eta^{(0)}_{xyt_1t_1}] \\ &- H_x\{-\eta^{(0)}_{xt_3} + \eta^{(0)}_{yt_1t_1} + \eta^{(0)}_{xt_1t_1t_1} - \eta^{(0)}_x\eta^{(0)}_{xy} \\ &+ [\eta^{(0)}_y + \eta^{(0)}_{xt_1}]\eta^{(0)}_{xx}\} + \eta^{(0)}\eta^{(0)}_{xxt_1} + \eta^{(0)}_x\eta^{(0)}_{xt_1}. \end{aligned} \tag{A20}$$

We look for a solution of this equation in the form $\eta^{(2)} = F^{(2)}(x)\Phi^{(2)}(ky - \omega t_1, t_3, \ldots)$. The t_1 derivatives should be replaced in Eq. (A20) by the y ones according to the rule $\partial_y = -k/\omega\,\partial_{t_1}$ consistent with the unidirectional propagation of the topographic waves. We thus get the following equation for $F^{(2)}(x)$:

$$\Phi^{(2)}_{t_1}\left[F^{(2)} + H_x\left(\frac{k}{\omega}F^{(2)} - F^{(2)}_x\right) - HF^{(2)}_{xx}\right] = \{\text{r.h.s}\}, \tag{A21}$$

where {r.h.s.} stands for the r.h.s. of Eq. (A20). By multiplying by $F^{(0)}(x)$ and integrating by x, we get the Korteweg–deVries equation for $\Phi^{(0)}$,

$$a\Phi^{(0)}_{t_3} + b\Phi^{(0)}_{yyy} + c\Phi^{(0)}\Phi^{(0)}_y = 0, \tag{A22}$$

where the coefficients are given by

$$a = \int_{-\infty}^{+\infty} F^{(0)}[-F^{(0)} + H_xF^{(0)}_x + HF^{(0)}_{xx}]dx, \tag{A23}$$

$$b = \int_{-\infty}^{+\infty} F^{(0)}\left[-H_x\left(\frac{\omega^2}{k^2}F^{(0)} - \frac{\omega^3}{k^3}F^{(0)}_x\right) - H\left(-\frac{\omega^3}{k^3}F^{(0)}_{xx} + \frac{\omega}{k}F^{(0)}\right)\right]dx, \tag{A24}$$

$$c = \int_{-\infty}^{+\infty} F^{(0)}\left[-H_x\left(-F^{(0)}_xF^{(0)}_x + F^{(0)}F^{(0)}_{xx} - \frac{\omega}{k}F^{(0)}_xF^{(0)}_{xx}\right) - H\left(F^{(0)}_xF^{(0)}_{xx} + F^{(0)}F^{(0)}_{xxx} - \frac{\omega}{k}(F^{(0)}_{xx}F^{(0)}_{xx} + F^{(0)}_xF^{(0)}_{xxx})\right) - \frac{\omega}{k}(F^{(0)}_xF^{(0)}_x + F^{(0)}F^{(0)}_{xx})\right]dx. \tag{A25}$$

The numerical values of a, b, and c may be easily found for any linear escarpment.

The appearance of the KdV equation for slow evolution of weakly nonlinear long topographic waves could be expected. Indeed, the dispersion of long unidirectionally propagating topographic waves is weak (cf. the dispersion curve Fig. 4) and may be compensated by weak nonlinearity to give solutions preserving their form, a typical situation in which the KdV equation arises.

Surprisingly, soliton-like structures in topographic waves arise at strong nonlinearities, as our numerical simulation shows. In this respect, again, the situation is similar to that observed in simulations of the equatorial adjustment.[12]

[1] A. E. Gill, M. K. Davey, E. R. Johnson, and P. F. Linden, "Rossby adjustment over a step," J. Mar. Res. **44**, 713 (1986).
[2] E. R. Johnson and M. K. Davey, "Free-surface adjustment and topographic waves in coastal currents," J. Fluid Mech. **219**, 273 (1990).
[3] S. E. Allen, "Rossby adjustment over a slope in a homogeneous fluid," J. Phys. Oceanogr. **26**, 1646 (1996).
[4] A. C. Kuo and L. M. Polvani, "Time-dependent fully nonlinear geostrophic adjustment," J. Phys. Oceanogr. **27**, 1614 (1997).
[5] C.-G. Rossby, "On the mutual adjustment of pressure and velocity distributions in certain simple current systems, ii," J. Mar. Res. **1**, 239 (1937).
[6] V. Zeitlin, S. B. Medvedev, and R. Plougonven, "Frontal geostrophic adjustment, slow manifold and nonlinear wave phenomena in one-dimensional rotating shallow water. Part 1: Theory," J. Fluid Mech. **481**, 269 (2003).
[7] F. Bouchut, J. LeSommer, and V. Zeitlin, "Frontal geostrophic adjustment and non-linear wave phenomena in one-dimensional rotating shallow water. Part 2: High resolution numerical simulations," J. Fluid Mech. **514**, 35 (2004).
[8] F. Bouchut, *Nonlinear Stability of Finite Volume Methods for Hyperbolic Conservation Laws, and Well-balanced Schemes for Sources*, Frontiers in Mathematics Series (Birkhaüser, Basel, 2004).
[9] F. Bouchut, "Efficient numerical finite-volume schemes for shallow water models" in *Nonlinear Dynamics of Rotating Shallow Water: Methods and Advances*, edited by V. Zeitlin, Edited Series on Advances in Nonlinear Science and Complexity (Elsevier, Amsterdam, 2007), pp. 191–258.
[10] G. M. Reznik, V. Zeitlin, and M. Ben Jelloul, "Nonlinear theory of geostrophic adjustment. Part 1: Rotating shallow water model," J. Fluid Mech. **445**, 93 (2001).
[11] M. S. Longuet-Higgins, "Double Kelvin waves with continuous depth profile," J. Fluid Mech. **34**, 49 (1968).
[12] J. LeSommer, G. M. Reznik, and V. Zeitlin, "Nonlinear geostrophic adjustment of long-wave disturbances in the shallow water model on the equatorial beta-plane," J. Fluid Mech. **515**, 135 (2004).
[13] F. Bouchut, J. Le Sommer, and V. Zeitlin, "Breaking of balanced and unbalanced equatorial waves," Chaos **15**, 013503 (2005).
[14] E. Audusse, F. Bouchut, M.-O. Bristeau, R. Klein, and B. Perthame, "A fast and stable well-balanced scheme with hydrostatic reconstruction for shallow water flows," SIAM J. Sci. Comput. (USA) **25**, 2050 (2004).
[15] P. H. LeBlond and L. A. Mysak, *Waves in the Ocean*, Elsevier Oceanography Series (Elsevier, Amsterdam, 1978).
[16] Note, however, that the exact value of the amplitude of the perturbation is not given in Ref. 3.
[17] Due to their above-mentioned balanced character, we find this name more appropriate than the double Kelvin waves.

[18]The diagnostic of transport with the help of potential vorticity frequently used in literature is not well suited for the present study because initial potential vorticity takes four different (constant) values out of the slope plus a continuous spectrum of values in the region of the slope.
[19]A. V. Fedorov and W. K. Melville, "Propagation and breaking of nonlinear Kelvin waves," J. Phys. Oceanogr. **25**, 2518 (1995).
[20]A. V. Fedorov and W. K. Melville, "Kelvin fronts on the equatorial thermocline," J. Phys. Oceanogr. **30**, 1692 (2000).
[21]G. F. Carnevale, S. G. Llewelyn-Smith, F. Crisciani, R. Purini, and R. Serraval, "Bifurcation of a coastal current at an excarpment," J. Phys. Oceanogr. **29**, 969 (1999).